

Article

Catalytic Hydrogenation of γ -Butyrolactone to Butanediol over a High-Performance Cu-SiO₂ Catalyst

Xiaoni Ren^{1,2}, Mo Zhou², Wenguang Yu³, Mingyuan Zheng^{2,3,*}  and Qingda An^{1,*}

¹ Faculty of Light Industry and Chemical Engineering, Dalian Polytechnic University, Dalian 116034, China; renxn@dicp.ac.cn

² CAS Key Laboratory of Science and Technology on Applied Catalysis, Dalian Institute of Chemical Physics, Chinese Academy of Sciences, Dalian 116023, China; zhouchoum@dicp.ac.cn

³ Dalian National Laboratory for Clean Energy, Division of Energy Research Resources, Dalian Institute of Chemical Physics, Chinese Academy of Sciences, Dalian 116023, China; wgyu@dicp.ac.cn

* Correspondence: myzheng@dicp.ac.cn (M.Z.); anqingda@dlpu.edu.cn (Q.A.)

Abstract: High-performance Cu catalysts were developed for the selective hydrogenation of γ -butyrolactone (GBL) to 1,4-butanediol (BDO). Among the various catalysts prepared by ammonia evaporation (AE) and impregnation (IM) methods with silica or MFI zeolite supports, the 5% Cu-SiO₂-AE catalyst was the best one. It exhibited 95% selectivity for BDO and 71% conversion of GBL after 2–8 h reaction at 200 °C and 4 MPa H₂, with high stability in five-cycle runs. Comprehensive characterizations showed that the AE method favored generating nano Cu particles with an average size of 2.9 nm on the 5% Cu-SiO₂-AE catalyst. The silica support derived from a sol demonstrated an advantage over the MFI zeolite in the preparation of a highly dispersed and stable Cu catalyst, in view of its anti-sintering and robust composition of Cu⁰, Cu⁺, and Cu²⁺ in the cycling operation. The reaction pathways for GBL to BDO over the Cu catalysts were found to commonly involve reversible reactions of hydrogenation and dehydrogenation, along with subsequent dehydration to form THF. The high performance of the Cu catalysts in the conversion of GBL to BDO was attributed to the high dispersion of Cu, the presence of stable active sites, and fewer strong acid sites in the catalyst.

Keywords: γ -butyrolactone; 1,4-butanediol; hydrogenation; copper; silica



Citation: Ren, X.; Zhou, M.; Yu, W.; Zheng, M.; An, Q. Catalytic

Hydrogenation of γ -Butyrolactone to Butanediol over a High-Performance Cu-SiO₂ Catalyst. *Catalysts* **2024**, *14*, 297. <https://doi.org/10.3390/catal14050297>

Academic Editors: Shihui Zou and Juanjuan Liu

Received: 30 March 2024

Revised: 24 April 2024

Accepted: 27 April 2024

Published: 29 April 2024



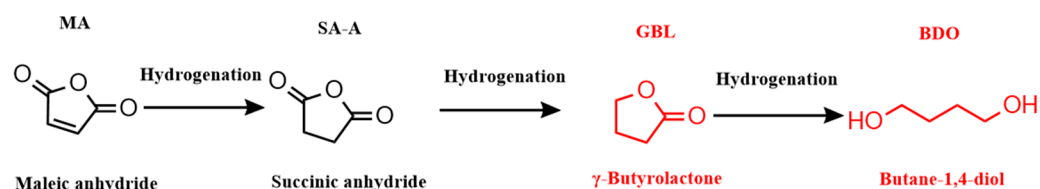
Copyright: © 2024 by the authors. Licensee MDPI, Basel, Switzerland. This article is an open access article distributed under the terms and conditions of the Creative Commons Attribution (CC BY) license (<https://creativecommons.org/licenses/by/4.0/>).

1. Introduction

As an important organic chemical and fine chemical feedstock, 1,4-butanediol (BDO) has been widely used in the synthesis of the degradable plastics polybutylene succinate (PBS) and polybutylene adipate terephthalate (PBAT) [1–3]. With the increasing appeal for restrictions on plastics, the global market demand for BDO is about 2.07 million tons, and it has been estimated that this will increase at a rate of 5–10% per year in the near future [4–7]. Currently, more than 95% of BDO is obtained using the acetylenic aldehyde method, which is energy-intensive and over-reliant on fossil energy resources [8–10]. Stimulated by the depletion of fossil resources and the demand for low-carbon and renewable chemical processes, the sustainable production of BDO is receiving more and more attention.

The catalytic hydrogenation of maleic anhydride to BDO (MATB) is a sustainable process, as the reactant can be obtained from the conversion of biomass platform compounds like butanol, furfural, and lignin [11–15]. The MATB process largely includes three reaction steps: maleic anhydride hydrogenation to succinic anhydride, then to γ -butyrolactone (GBL), and the final product of BDO, as depicted in Scheme 1 [16–18]. In the past decades, remarkable progress has been achieved in producing BDO from succinic acid. For example, Minh et al. reported that ca. 60% selectivity and yield of BDO from succinic acid were obtained over supported bimetallic 4%Re-2%Pd/C catalysts at 160 °C under a pressure of 150 bar [19,20]. Benoit et al. claimed that the BDO yield was related to the oxidation state of the Re³⁺ rather than Re⁰ species over the Re-Pd/TiO₂ catalysts. Ki Hyuk et al. reported

that the yield of BDO was well correlated with the number of weak hydrogen-binding sites of the Re catalysts [21,22]. Cheaper metals like Cu and Fe have been used to replace noble metals and construct bimetallic M_1 - M_2 /C catalysts (where M_1 and M_2 are base and noble metals, respectively) to realize catalytic conversion of succinic acid to BDO under milder reaction conditions [23–25]. For instance, Son et al. reported a 8Cu-2Pd/HAP catalyst, which afforded 82% BDO selectivity after 96 h reaction at 200 °C and 8 MPa H_2 [4]. Additionally, there have been reports indicating that Cu-based catalysts can facilitate the synthesis of BDO under light irradiation [26–29].



Scheme 1. Reaction pathways for catalytic hydrogenation of MA into BDO.

As illustrated in Scheme 1, GBL is a critical intermediate for BDO formation. It can be obtained from maleic anhydride hydrogenation, as shown in our previous study [30]. Compared to succinic acid, it is a better feedstock in view of its higher selectivity for BDO and the less expensive catalysts used in its conversion. Huber et al. obtained ca. 90% selectivity in GBL conversion to BDO over a Cu-Co/TiO₂ catalyst [31]. Therefore, a high performance catalyst for GBL conversion to BDO is a very attractive prospect for the MTAB process.

Herein, we synthesized a set of Cu catalysts by ammonia evaporation (AE) and impregnation (IM) methods using silica or MFI zeolite as the supports, and then applied them in the hydrogenation of GBL to BDO. In comparison to the Cu catalysts supported on the MFI zeolite, the catalytic performance of Cu-SiO₂-AE was significantly outstanding. Under reaction conditions of 180 °C and 4 MPa H_2 , excellent selectivity of 95.8% towards BDO was obtained on the 5%Cu-SiO₂-AE catalyst. Moreover, the catalyst showed stable catalytic performance in at least five consecutive reaction cycles. Systematic characterizations were conducted to identify the structures and properties of the Cu catalysts, which accounted for their performance in GBL hydrogenation to BDO.

2. Results and Discussion

2.1. Catalytic Performance in GBL Hydrogenation

We first compared the catalytic performance of several typical base metal (Ni, Co, and Cu) catalysts often used in hydrogenation reactions [30,32]. From the results shown in Figure 1a, both the Co and Ni-MFI-AE catalysts showed a remarkably high selectivity for tetrahydrofuran (THF, 40–50%), but the BDO selectivity was as low as <5%. According to our previous study [30], the 40Ni-MFI catalyst presented a remarkable amount of medium-strength acid sites, which may account for the high selectivity for THF in the reaction. In contrast, over the 40%Cu-MFI-AE catalyst, 53.2% selectivity for BDO was obtained. In addition, it should be noted that in terms of the widely used noble metal catalysts 5%Pd/C and 5%Ru/C, they did not show notable reaction activity and were much more inert as compared with the Cu catalyst (Table S1). Therefore, copper was used as the suitable active component for catalyst optimization.

The effects of Cu loading, the silicious supports, and the preparation methods of the catalysts on the reaction performance were investigated (Figures S1–S4). The best catalytic performance was observed over the 5%Cu-SiO₂-AE catalyst, which afforded 95.8% selectivity for BDO and 61.7% GBL conversion, with an atom economy of 98%, referring to the method in the literature [33]. The MFI zeolite-supported Cu catalysts showed notably lower BDO selectivity but much higher yields of THF as compared to the SiO₂-supported catalysts (Figure 1b). In view of the higher yield of BDO over the catalyst, the AE method exhibited an advantage over the IM method in the preparation of a robust Cu catalyst

shown in Figure 2b,d, demonstrating that the support property had a more significant effect on the catalyst stability. In our previous study, Cu-MFI-AE catalysts were robust in ethanol dehydrogenation [34]. However, in the present study, the 5%Cu-SiO₂-AE catalyst was the notably better one, indicating that the silicious support derived from a silica sol is an attractive candidate for the synthesis of a high performance catalyst.

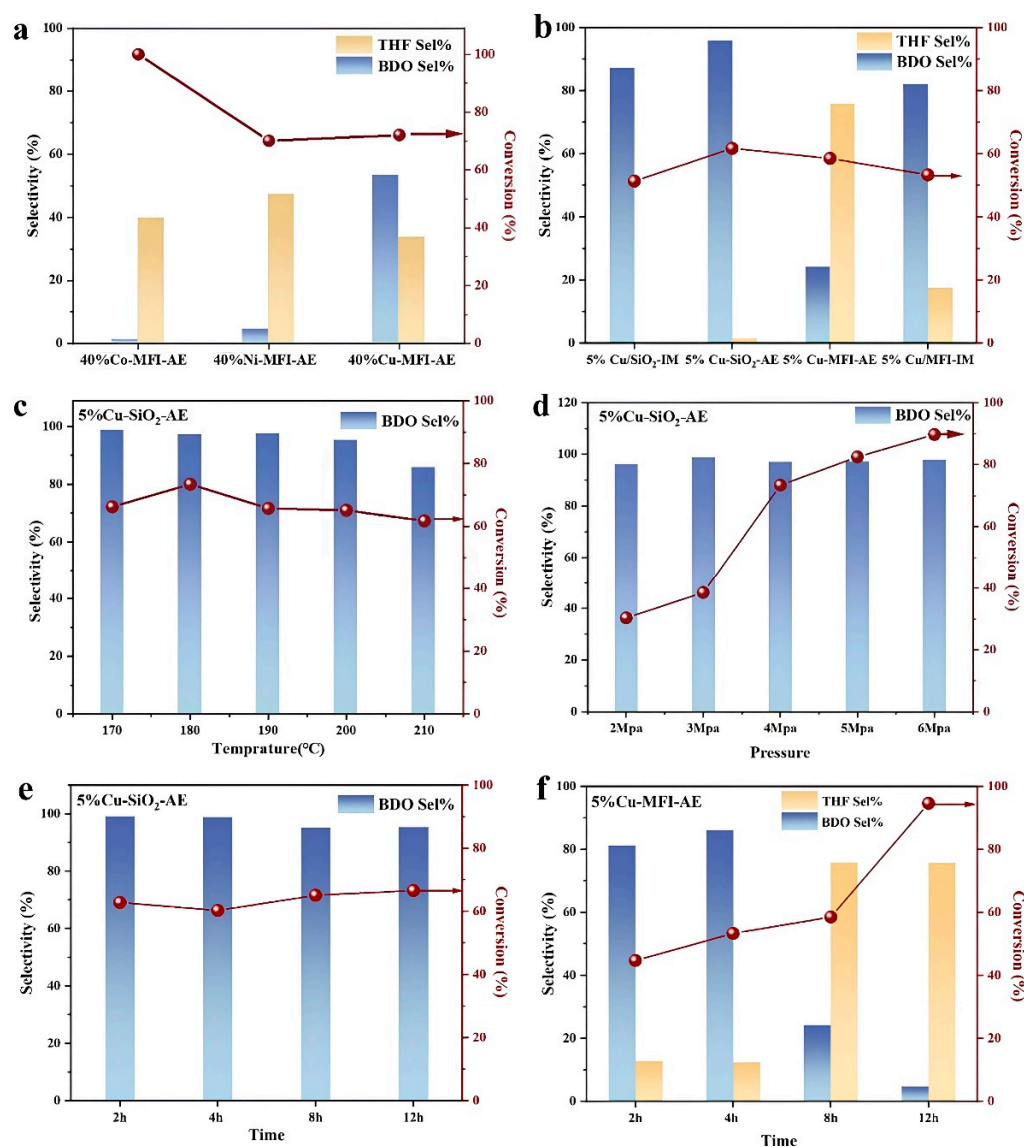


Figure 1. (a) Catalytic performance of GBL hydrogenation over various base metal catalysts ($T = 200\text{ }^{\circ}\text{C}$, 4 MPa H₂, 8 h); (b) results of GBL hydrogenation over different Cu catalysts ($T = 200\text{ }^{\circ}\text{C}$, 4 MPa H₂, 8 h); performance of 5%Cu-SiO₂-AE catalyst for GBL hydrogenation at (c) different temperatures (4 MPa H₂, 8 h) and (d) H₂ pressures ($T = 200\text{ }^{\circ}\text{C}$, 8 h); (e) performance of 5%Cu-SiO₂-AE catalyst for GBL hydrogenation at different times ($T = 200\text{ }^{\circ}\text{C}$, 4 MPa H₂); (f) performance of 5%Cu-MFI-AE catalyst for GBL hydrogenation at different times ($T = 200\text{ }^{\circ}\text{C}$, 4 MPa H₂).

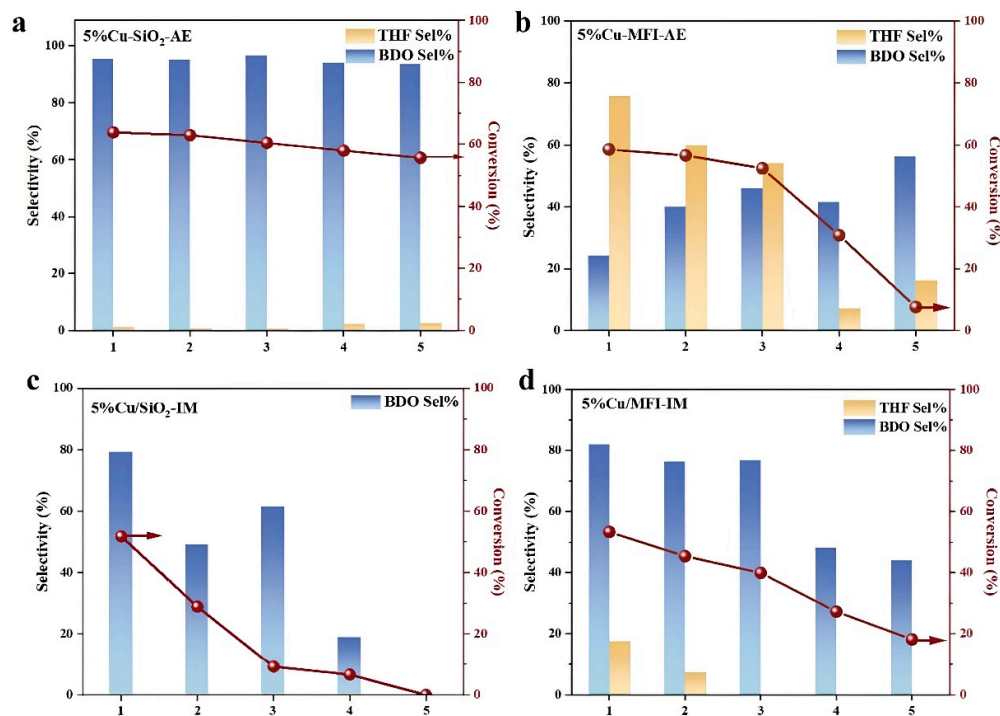


Figure 2. Results of cycling experiments for 5%Cu-SiO₂-AE catalyst (a), 5%Cu-MFI-AE catalyst (b), 5%Cu/SiO₂-IM catalyst (c), and 5%Cu/MFI-IM catalyst (d). Reaction conditions: T = 200 °C, 4 MPa H₂, 8 h.

2.2. Catalysts Characterizations and Discussion

The physicochemical properties of the various Cu catalysts were characterized by N₂ adsorption and are shown in Figure S9 and Table S2. Both the MFI- and SiO₂-supported Cu catalysts had large specific surface areas of 260–380 m²/g. The pristine microporous structure of MFI was well retained ($S_{\text{micro}} = 194.3 \text{ m}^2/\text{g}$) after loading Cu species onto the 5%Cu/MFI-IM catalyst by the IM method. However, synthesizing the 5%Cu-SiO₂-AE catalyst by the AE method generated remarkable amounts of mesopores with an average size of 6.8 nm at the expense of micropores. Different from the MFI- and zeolite-supported catalysts, the two SiO₂-supported Cu catalysts only contained large mesopores, ranging in size from 5–20 nm, which afforded an abundant ($S_{\text{ext}} = 250\text{--}370 \text{ m}^2/\text{g}$) external surface.

The X-ray diffraction (XRD) patterns of various reduced Cu catalysts are displayed in Figure 3. The typical peaks owing to the crystallite nature of MFI zeolite were clearly observed in the XRD patterns of the MFI-supported Cu catalysts, demonstrating that zeolite was synthesized successfully and that its structure was retained well after loading Cu on it. As for the diffraction peaks of metallic Cu, they were observed on the patterns of the Cu/MFI-IM and Cu/SiO₂-IM catalysts, but absent for those prepared by the AE method. This suggests the latter two catalysts contained more uniformly dispersed copper species [35,36]. For the spent 5%Cu-SiO₂-AE catalyst (after five times running), no sign of bulk metallic Cu particles was observed. This demonstrates that the copper species on the 5%Cu-SiO₂-AE catalyst are stable and not apt to sinter during the reaction, possibly owing to the enhanced interaction between Cu and the silicious supports in the AE process [34,37].

The HAADF-STEM images of 5%Cu-SiO₂-AE and 5%Cu-MFI-AE catalysts showed the metal dispersion on the supports (Figures 4 and 5). The metallic Cu nanoparticles were finely distributed on the silicious support, with average sizes of about 2.9 and 8.7 nm for the 5%Cu-SiO₂-AE and 5%Cu-MFI-AE catalysts, respectively. Moreover, the 5%Cu-SiO₂-AE catalyst displayed a morphology consisting of uniformly packed spheres ca. 10 nm in size, which accounted for the mesoporous structures in the catalyst. After five-cycle reactions, the sizes of the metallic Cu nanoparticles and SiO₂ nanospheres barely changed in the 5%Cu-SiO₂-AE catalyst (Figure S10), in line with its high stability in catalytic performance.

On the contrary, the average size of the Cu nanoparticles over 5%Cu-MFI-AE significantly grew from 8.7 to 29.1 nm (Figure S11) after five cycles of use, consistent with the rapid deactivation in the cycling experiments.

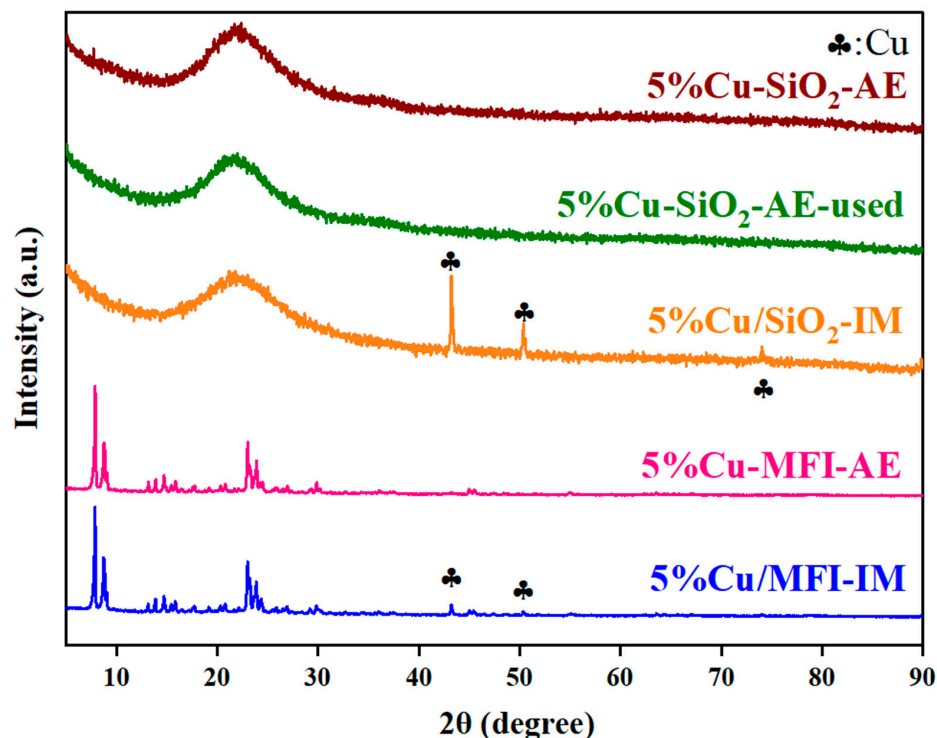


Figure 3. XRD patterns for the typical as-prepared Cu catalysts and the spent catalyst.

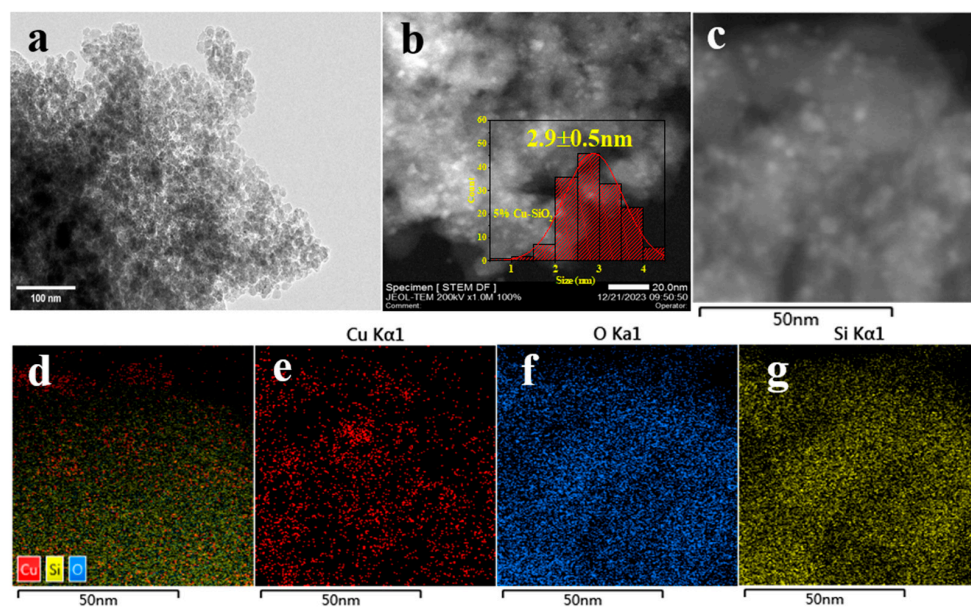


Figure 4. TEM image (a), HAADF-STEM images (b,c), and element mapping images (d–g) of 5%Cu-SiO₂-AE catalyst.

H₂-TPR experiments were conducted to probe the state of Cu species on the various catalysts before reduction. As illustrated in Figure 6, a sharp H₂ consumption peak was observed at 204 °C for the 5%Cu-SiO₂-AE catalyst, which was attributed to the highly dispersed Cu species on the silicious support [34,38–40]. The 5%Cu-MFI-AE catalyst presented a similar reduction peak at 207°, but with a wider scope of temperature than that

of the 5%Cu-SiO₂-AE counterpart. This indicates that the Cu species distribution on the 5%Cu-MFI-AE catalyst was less uniform than that over the 5%Cu-SiO₂-AE catalyst [41,42], consistent with the HAADF-STEM observation. As for the reduction behaviors of the Cu/MFI-IM and Cu/SiO₂-IM catalysts, H₂ consumption peaks at notably higher temperatures (ca. 300 °C) were observed. This indicates that bulk CuO particles were present in the catalyst precursors [43–45], which formed large size metallic Cu particles after reduction, as evidenced by the XRD analysis.

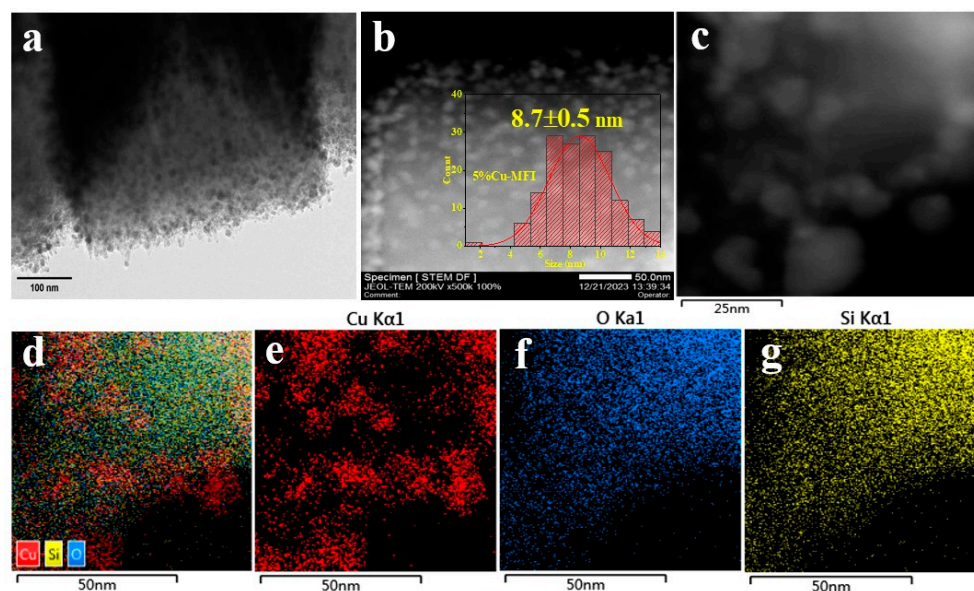


Figure 5. TEM image (a), HAADF-STEM images (b,c), and element mapping images (d–g) of 5%Cu-MFI-AE catalyst.

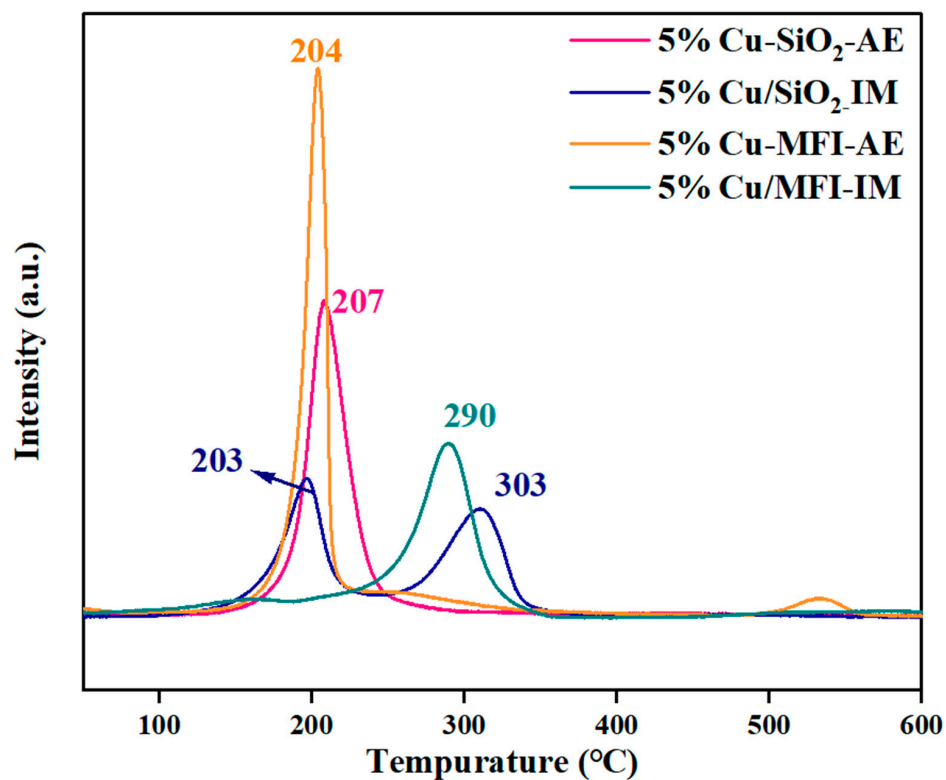


Figure 6. H₂-TPR profiles for the typical Cu catalysts.

Pyridine-FTIR experiments were conducted to measure the nature of the acid sites over the catalysts. As displayed in Figure 7a, bands at 1450 and 1609 cm^{-1} , owing to Lewis acid sites (LAS), were observed over the Cu catalysts [46–48]. The strength of catalyst acidity was probed by NH_3 -TPD-MS measurements and the results are displayed in Figure 7b. NH_3 desorption occurred in the range of 100–400 $^{\circ}\text{C}$ for all of the Cu catalysts, indexed to the weak and medium-strong acid sites [49,50]. Among the various catalysts, 5%Cu-SiO₂-AE showed the lowest amount of medium-strong acid sites, according to its NH_3 desorption peak area at 288 $^{\circ}\text{C}$ [51]. The amounts of medium-strong acid sites follow an order of 5%Cu-MFI-AE > 5%Cu/MFI > 5Cu/SiO₂ > 5%Cu-SiO₂-AE, which is well in line with the trend of THF selectivity observed over the four catalysts. Therefore, the strong acidity of catalysts facilitates the dehydration of BDO to form THF.

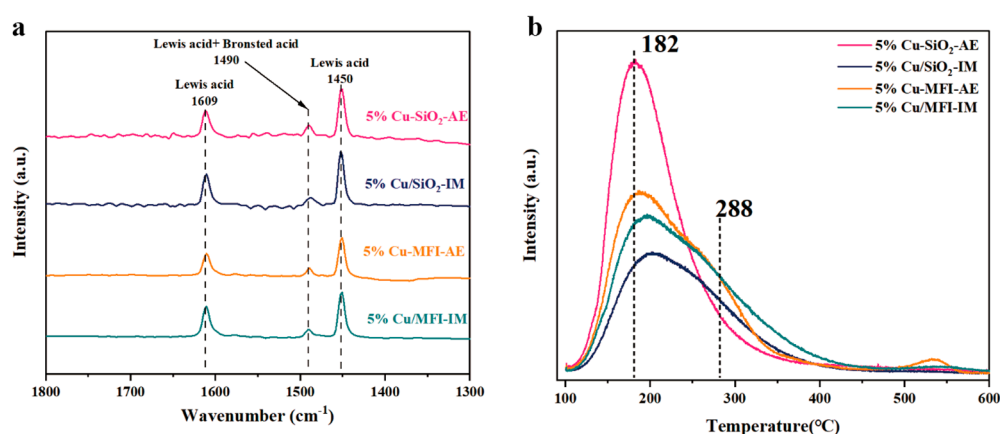


Figure 7. (a) Py-FTIR spectra of the typical Cu catalysts, (b) NH_3 -TPD profiles for the various Cu catalysts.

It has been reported that the chemical state of metal species affects hydrogenation activity. Therefore, XPS analysis was employed to identify the valence state of the Cu species on the catalysts (Figure 8). The different Cu species were distinguished and quantified by deconvoluting the XPS peaks. The signals at 932.8 and 952.7 eV were assigned to the Cu 2p_{1/2} and 2p_{3/2} of the reduced Cu species (Cu⁰ and/or Cu⁺), respectively, which were observed over all the Cu catalysts [52,53]. The XAES of Cu LMM analysis provided quantified information regarding the Cu⁺ (913.7 eV) and Cu⁰ (916.9 eV) species composition (Figures S12 and S13) according to the integral areas [41,52,54]. The relative contents of the Cu species in various valences are displayed in Figure 9. Over the fresh 5%Cu-SiO₂-AE catalyst, 20% of Cu was completely reduced to the metallic state and remained in the catalyst, along with 55% oxidic Cu⁺ and 25% oxidic Cu²⁺. After five repeated cycles, the composition of Cu in different valences did not notably change, manifesting the high stability of the 5%Cu-SiO₂-AE catalyst in the reactions. Similar stability in the Cu species composition was also observed on the 5%Cu-MFI-AE catalyst after five cycles of operation. Again, this shows that the active Cu species on the catalysts prepared by the AE method were relatively stable. On the contrary, the valence of the Cu species in the Cu catalysts prepared by the IM method changed significantly after cyclic reactions, with a notable increase in the Cu²⁺ content and a decrease in the Cu⁺ content. Thus, the instability of the Cu species over the catalysts may partially account for the deactivation of IM method-prepared Cu catalysts in cyclic reactions.

In addition, it should be noted that there may be a synergistic effect between Cu⁺ and Cu⁰ species in GVL hydrogenation. According to a previous study on the dehydrogenation of ethanol to acetaldehyde, Cu⁺ sites were deemed to play critical roles in alcohol activation and dehydrogenation to form a reaction intermediate, and then the Cu⁰ sites promoted the combination of hydrogen atoms to form H₂, thereafter releasing it from the catalyst surface. In view of the hydrogenation of GVL to BDO following a reversible reaction route, it is

reasonable to assume that Cu⁺ and Cu⁰ sites may jointly contribute to the reaction. Moreover, some studies have found that the Cu⁺ species plays a crucial role in ester molecule adsorption and activation, and determines the rate of dimethyl oxalate hydrogenation. A proper Cu⁰/Cu⁺ molar ratio can dramatically improve catalytic activity [55,56]. Therefore, a similar synergistic effect between the Cu⁰ and Cu⁺ sites might occur in the present study of GBL to BDO.

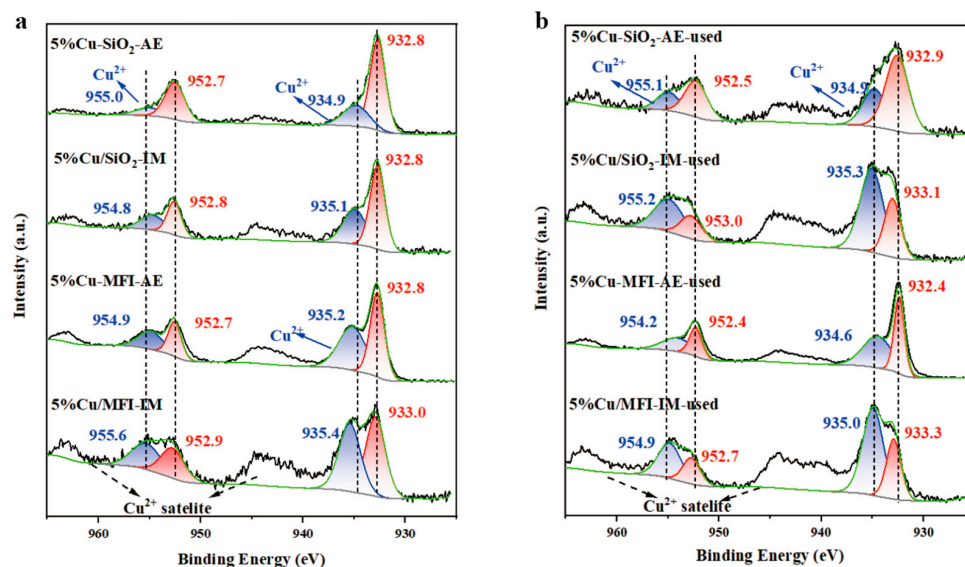


Figure 8. XPS spectra for the fresh (a) and the spent (b) Cu catalysts.

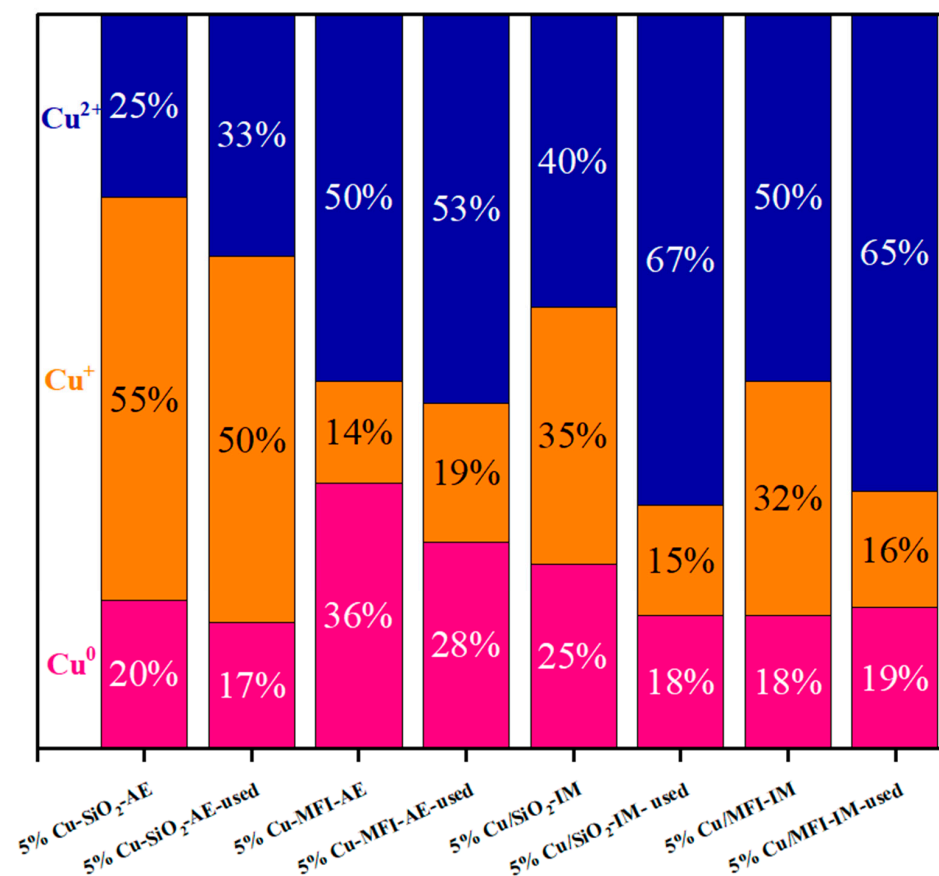


Figure 9. The various Cu species contents in the fresh and spent Cu catalysts, according to the XPS results.

3. Materials and Methods

3.1. Catalyst Preparation

All reagents were commercially purchased without further purification. Copper nitrate hexahydrate, ammonia solution (25 wt%), γ -butyrolactone (GBL, 99% AR), 1,4-butanediol (BDO, 99% AR), and a sol of SiO₂ were purchased from Sinopharm Chemical Reagent Co., Ltd. (Shanghai, China). Tetrapropylammonium hydroxide (TPAOH, 25 wt% solution) was purchased from Energy Chemical Co., Ltd. (Weinan, China). Tetraethyl orthosilicate (TEOS, 98% AR) and 1,4-dioxane (1,4-DOX, 99.5% AR) were purchased from Xilong Science Co., Ltd. (Shantou, China). The commercial silica SiO₂ was purchased from Qingdao Haiyang Co., Ltd. (Qingdao, China).

Synthesis of MFI Support: In a typical procedure, TEOS and TPAOH were added into deionized water at a molar ratio of 1.0 TEOS: 0.5 TPAOH: 30 H₂O, as described in our previous work [57,58]. The solution was continuously stirred in a beaker for 3 h, and then transferred to a Teflon lined stainless steel autoclave at 160 °C for 48 h. The obtained solid was centrifuged, washed with deionized water, and dried overnight at 100 °C. Finally, the solid was calcined at 550 °C for 4 h to remove organic impurities.

Synthesis of Cu-SiO₂-AE and Cu-MFI-AE: The Cu-SiO₂-AE and Cu-MFI-AE catalysts were prepared by the ammonia evaporation (AE) method [37,59]. In a typical procedure, a certain amount of copper nitrate (Cu(NO₃)₂) was dissolved in 100 mL of water to obtain a solution (0.08 mol/L) in a 500 mL beaker. Ammonium hydroxide (25 wt% NH₃-H₂O) was added at a 1:9 molar ratio to Cu, followed by the addition of 10 g of corresponding support (sol-SiO₂ or MFI). The mixture was stirred continuously for 6 h and ammonia was evaporated at 80 °C for 6 h. When the pH of the solution decreased to ca. 7, the evaporation process was terminated. Then, the solid was washed, filtered, and dried at 100 °C for 12 h. Finally, the sample was calcined at 400 °C for 4 h at a heating rate of 5 °C/min. The as-prepared catalyst precursor was subsequently reduced at 300 °C in a 5% H₂/N₂ flow for 1 h at a heating rate of 5 °C/min, and named as 5%Cu-SiO₂-AE or 5%Cu-MFI-AE, indicating a Cu loading of 5 wt% on Cu-SiO₂-AE or Cu-MFI-AE catalyst prepared by the AE method. Other transition metal (Ni and Co) catalysts were also prepared following the same procedure, except the metal salts were changed to the counterparts of nitrates.

Synthesis of Cu/SiO₂-IM and Cu/MFI-IM: The Cu/SiO₂-IM and Cu/MFI-IM catalysts were prepared using the impregnation (IM) method. A certain amount of 0.08 mol/L Cu(NO₃)₂ solution was dropped into 10 g of the corresponding support (commercial silica SiO₂ or MFI) for 12 h. Then, the samples were dried at 100 °C for 12 h, calcined at 400 °C in static air for 4 h, and subsequently reduced at 300 °C in a 5% H₂/N₂ flow for 1 h at a heating rate of 5 °C/min. The catalysts were named as 5%Cu/SiO₂-IM and 5%Cu/MFI-IM.

3.2. Reaction Process

The liquid-phase hydrogenation of GBL was carried out in a high-pressure batch reactor at 170–210 °C and 2–6 Mpa H₂ for 8 h. Typically, the catalyst (0.1 g) and 19 g solution of 5% GBL in 1,4-dioxane were placed in a 100 mL batch reactor. After the air was expelled, 4 MPa H₂ was charged into the reactor and stirred at 800 rpm. Then, the reactor was heated to the reaction temperature. After reaction, the reactor was cooled to room temperature, and the composition of the supernatant was analyzed by a gas chromatograph (GC, Agilent 7890A, Palo Alto, CA, USA) equipped with an FFA (30 m × 0.32 mm × 1.0 μm) capillary column and a flame ionization detector (FID).

The selectivity of the GBL conversion and products were calculated according to the following equations:

$$\text{GBL Conversion (\%)} = \frac{\text{mole of GBL charged} - \text{mole of GBL left}}{\text{mole of GBL charged}} \times 100$$

$$\text{Product Selectivity (\%)} = \frac{\text{mole of product}}{\text{mole of GBL charged} - \text{mole of GBL left}} \times 100$$

3.3. Catalyst Characterization

X-ray powder diffraction (XRD) analysis was conducted using a PANalytical XPert-Pro powder X-ray diffractometer equipped with Cu-K α monochromatic radiation ($\lambda = 0.1541$ nm) operating at 40 kV and 40 mA.

N₂ adsorption and desorption experiments were conducted on a Micromeritics ASAP 2460 system at -196 °C.

Transmission electron microscopy (TEM) images, scanning transmission electron microscopy (STEM) images, and energy-dispersive X-ray spectroscopy (EDS) elemental mapping of samples were obtained using a JEM-2100F microscope (JEOL, Tokyo, Japan) operating at 200 kV.

H₂ temperature-programmed reduction (H₂-TPR) was conducted on a Micromeritics Autochem II equipped with a TCD detector. Typically, 100 mg of the sample underwent pretreatment at 300 °C for 1 h in an Ar flow of 30 mL/min. After cooling to 50 °C for stabilization, the TCD signal was monitored while heating the sample to 900 °C at a rate of 10 °C/min in a 30 mL/min H₂ flow.

NH₃ temperature-programmed desorption (NH₃-TPD) was conducted on a Micromeritics Autochem II apparatus equipped with a mass spectrometer (MS) detector.

The acidity of the catalysts was assessed by infrared spectra of pyridine adsorption using a Bruker Tensor 27 instrument (Bruker, Billerica, MA, USA). The acid density was calculated by the equation: pyridine on Lewis acid sites = $1.42 \text{ IA(L)R}^2 / W$, where IA (Lewis acid sites) = integrated absorbance of Lewis acid bands (cm^{-1}), R = radius of catalyst disk (cm), and W = weight of catalyst (mg).

X-ray photoelectron spectra (XPS) were collected on a Thermo Scientific K-Alpha⁺ spectrometer (XPS Thermo Fisher Scientific, Waltham, MA, USA), with a monochromatic Al-K α X-ray source as the excitation source.

4. Conclusions

In this contribution, a high-performance Cu catalyst for GBL hydrogenation to BDO was developed using the AE method. Over the optimal 5%Cu-SiO₂-AE catalyst, BDO was obtained with 95% selectivity and 71% GBL conversion was achieved after 2–8 h reaction at 200 °C and 4 MPa H₂. The catalyst showed outstandingly high stability over at least five cycles of operation without any evident decline in reaction selectivity or catalyst activity. The TEM, XRD, and H₂-TPR analyses showed that the AE method is superior to the IM method for obtaining a highly dispersed Cu catalyst, i.e., 5%Cu-SiO₂-AE, over which the size of Cu nanoparticles centered at 2.9 nm. Compared to MFI zeolite, the silicious support derived from silica sol was more favorable for generating stable and nano-sized Cu catalysts via the AE method. The XPS analysis showed that Cu⁰, Cu⁺, and Cu²⁺ species existed on all of the as-prepared catalysts. Compared to the IM method-prepared catalysts, the AE method-prepared 5%Cu-SiO₂-AE catalyst more likely kept the composition of various Cu species intact during the cycling experiments, in line with the high stability of the catalyst. The reaction pathways for GBL to BDO over the Cu catalysts commonly involved reversible reactions of hydrogenation and dehydrogenation, and were followed by dehydration to form THF. The former is the major reaction and is progressed by higher pressures of H₂, while the latter readily happens in the presence of strong acid sites. A high dispersion of Cu species, the presence of stable active sites endowed by the AE method, and the presence of less strong acid sites on the catalyst were the major factors which determined the high performance of 5%Cu-SiO₂-AE in the conversion of GBL to BDO.

Supplementary Materials: The following supporting information can be downloaded at: <https://www.mdpi.com/article/10.3390/catal14050297/s1>, Figure S1: Catalytic performance of Cu-MFI-AE with different Cu loadings for GBL hydrogenation conversion to BDO (T = 200 °C, 4 MPa H₂, 8 h); Figure S2: Catalytic performance of Cu-SiO₂-AE catalysts with different Cu loadings for GBL hydrogenation conversion to BDO (T = 200 °C, 4 MPa H₂, 8 h); Figure S3: Catalytic performance of Cu/SiO₂-IM catalysts with different Cu loadings for GBL hydrogenation conversion to BDO (T = 200 °C, 4 MPa

H₂, 8 h); Figure S4: Catalytic performance of Cu/MFI-IM catalysts with different Cu loadings for GBL hydrogenation conversion to BDO (T = 200 °C, 4 MPa H₂, 8 h); Figure S5: Arrhenius plots of GBL conversion over 5%Cu-SiO₂-AE catalysts. The reaction conditions: GBL (1 g), 1,4-dioxane (19 mL), catalyst (0.1 g), The pressure of H₂ was 4 MPa, the reaction time was 30 min at different temperatures; Figure S6: Arrhenius plots of GBL conversion over 5%Cu/SiO₂-IM catalysts The reaction conditions: GBL (1 g), 1,4-dioxane (19 mL), catalyst (0.1 g), The pressure of H₂ was 4 MPa, the reaction time was 30 minutes at different temperatures; Figure S7: Catalytic performance of 5%Cu-SiO₂-AE catalyst for BDO reactions at different time (T = 200 °C, 4 MPa H₂); Figure S8: Catalytic performance of 5%Cu-MFI-AE catalyst for BDO reactions at different time (T = 200 °C, 4 MPa H₂); Figure S9: N₂ adsorption-desorption isotherms (a) and the corresponding pore size distributions (b) for the typical Cu catalysts; Figure S10: TEM image (a), HAADF-STEM images (b,c) and element mapping (d–g) of spent 5%Cu-SiO₂-AE catalyst; Figure S11: TEM image (a), HAADF-STEM images (b,c) and element mapping (d–g) of spent 5%Cu-MFI-AE catalyst; Figure S12: Cu LMM XPS spectra of the typical Cu catalysts; Figure S13: Cu LMM XPS spectra of the spent typical Cu catalysts; Table S1: Catalytic performance of 5%Pd/C and 5%Ru/C. Reaction conditions: T = 200 °C, 4 MPa H₂, 8 h; Table S2: Textural properties of the typical Cu-based catalysts.

Author Contributions: Data curation, X.R.; formal analysis X.R., M.Z. (Mo Zhou) and W.Y.; supervision, Q.A. and M.Z. (Mingyuan Zheng); writing—original draft, X.R.; writing—review and editing, Q.A. and M.Z. (Mingyuan Zheng) All authors have read and agreed to the published version of the manuscript.

Funding: This work was supported by “Transformational Technologies for Clean Energy and Demonstration”, Strategic Priority Research Program of the Chinese Academy of Sciences (XDA 21060200).

Data Availability Statement: The data is included in the article or Supplementary Materials.

Conflicts of Interest: The authors declare no conflict of interest.

References

1. Wu, J.; Gao, G.; Li, Y.; Sun, P.; Wang, J.; Li, F. Highly chemoselective hydrogenation of lactone to diol over efficient copper-based bifunctional nanocatalysts. *Appl. Catal. B Environ.* **2019**, *245*, 251–261. [[CrossRef](#)]
2. Zeng, F.; Hohn, K.L. Catalytic Conversion of Biomass-derived Compounds to C₄ Chemicals. *Catalysis* **2019**, *31*, 346. [[CrossRef](#)]
3. Liu, H.; Liu, S.; Ning, Y.; Zhang, R.; Deng, L.; Wang, F. Metabolic engineering of *Escherichia coli* for efficient production of 1,4-butanediol from crude glycerol. *J. Environ. Chem. Eng.* **2024**, *12*, 111660. [[CrossRef](#)]
4. Le, S.D.; Nishimura, S. Highly Selective Synthesis of 1,4-Butanediol via Hydrogenation of Succinic Acid with Supported Cu–Pd Alloy Nanoparticles. *ACS Sustain. Chem. Eng.* **2019**, *7*, 18483–18492. [[CrossRef](#)]
5. Ly, B.K.; Tapin, B.; Epron, F.; Pinel, C.; Especel, C.; Besson, M. In situ preparation of bimetallic ReOx-Pd/TiO₂ catalysts for selective aqueous-phase hydrogenation of succinic acid to 1,4-butanediol. *Catal. Today* **2020**, *355*, 75–83. [[CrossRef](#)]
6. Zhuang, J.; Yan, S.; Zhang, P.; Liu, X.; Zhao, Y.; Yu, Y.; Wang, Y.; Zhao, Q.; Wu, H.; Zhu, X.; et al. Regulating the states of Ni species by controlling the silanols of MCM-41 support to promote the hydrogenation of maleic anhydride. *Fuel* **2023**, *335*, 127030. [[CrossRef](#)]
7. Trotter, C.L.; Babu, G.S.; Wallace, S. Engineering biology for sustainable 1,4-butanediol synthesis. *Trends Biotechnol.* **2023**, *41*, 286–288. [[CrossRef](#)] [[PubMed](#)]
8. Li, F.; Lu, T.; Chen, B.; Huang, Z.; Yuan, G. Pt nanoparticles over TiO₂–ZrO₂ mixed oxide as multifunctional catalysts for an integrated conversion of furfural to 1,4-butanediol. *Appl. Catal. A Gen.* **2014**, *478*, 252–258. [[CrossRef](#)]
9. Li, K.; Yang, J.; Song, T.; Zhu, Z.; Zhao, C.; Wu, P.; Li, X. Synthesis of bio-derived 1,4-butanediol by succinic acid esterification and hydrogenation over CuFeAl catalysts. *Green Chem.* **2023**, *25*, 627–638. [[CrossRef](#)]
10. Zhu, Y.; Yang, J.; Mei, F.; Li, X.; Zhao, C. Bio-based 1,4-butanediol and tetrahydrofuran synthesis: Perspective. *Green Chem.* **2022**, *24*, 6450–6466. [[CrossRef](#)]
11. Liu, H.; Jiang, Y.; Zhao, H.; Hou, Z. Preparation of highly dispersed Cu catalysts from hydrotalcite precursor for the dehydrogenation of 1,4-butanediol. *J. Ind. Eng. Chem.* **2021**, *102*, 251–259. [[CrossRef](#)]
12. Patil, K.N.; Prasad, D.; Manoorkar, V.K.; Bhanushali, J.T.; Jadhav, A.H.; Nagaraja, B.M. Selective vapour-phase dehydrocyclization of biomass-derived 1,4-butanediol to γ -butyrolactone over Cu/ZnAl₂O₄-CeO₂ catalyst. *J. Ind. Eng. Chem.* **2022**, *106*, 142–151. [[CrossRef](#)]
13. Weidener, D.; Leitner, W.; Dominguez de Maria, P.; Klose, H.; Grande, P.M. Lignocellulose fractionation using recyclable phosphoric acid: Lignin, cellulose, and furfural production. *ChemSusChem* **2021**, *14*, 909–916. [[CrossRef](#)] [[PubMed](#)]
14. Zuliani, A.; Kikhtyanin, O.; Cova, C.M.; Rodriguez-Padron, D.; Kubička, D.; Luque, R. Boosting the Ni-Catalyzed Hydrodeoxygenation (HDO) of Anisole Using Scrap Catalytic Converters. *Adv. Sustain. Syst.* **2022**, *6*, 2100394. [[CrossRef](#)]

15. Weidener, D.; Klose, H.; von Westarp, W.G.; Jupke, A.; Leitner, W.; De Maria, P.D.; Grande, P.M. Selective lignin fractionation using CO₂-expanded 2-methyltetrahydrofuran (2-MTHF). *Green Chem.* **2021**, *23*, 6330–6336. [[CrossRef](#)]
16. Wang, T.; Liu, S.; Tamura, M.; Nakagawa, Y.; Hiyoshi, N.; Tomishige, K. One-pot catalytic selective synthesis of 1,4-butanediol from 1,4-anhydroerythritol and hydrogen. *Green Chem.* **2018**, *20*, 2547–2557. [[CrossRef](#)]
17. Gong, Z.-J.; Li, Y.-R.; Wu, H.-L.; Lin, S.D.; Yu, W.-Y. Direct copolymerization of carbon dioxide and 1,4-butanediol enhanced by ceria nanorod catalyst. *Appl. Catal. B Environ.* **2020**, *265*, 118524. [[CrossRef](#)]
18. Duan, H.; Hirota, T.; Ohtsuka, S.; Yamada, Y.; Sato, S. Vapor-phase catalytic dehydration of 1,4-butanediol to 3-buten-1-ol over modified ZrO₂ catalysts. *Appl. Catal. A Gen.* **2017**, *535*, 9–16. [[CrossRef](#)]
19. Minh, D.P.; Besson, M.; Pinel, C.; Fuertes, P.; Petitjean, C. Aqueous-Phase Hydrogenation of Biomass-Based Succinic Acid to 1,4-Butanediol Over Supported Bimetallic Catalysts. *Top. Catal.* **2010**, *53*, 1270–1273. [[CrossRef](#)]
20. Ly, B.K.; Minh, D.P.; Pinel, C.; Besson, M.; Tapin, B.; Epron, F.; Especel, C. Effect of Addition Mode of Re in Bimetallic Pd–Re/TiO₂ Catalysts Upon the Selective Aqueous-Phase Hydrogenation of Succinic Acid to 1,4-Butanediol. *Top. Catal.* **2012**, *55*, 466–473. [[CrossRef](#)]
21. Tapin, B.; Epron, F.; Especel, C.; Ly, B.K.; Pinel, C.; Besson, M. Influence of the Re introduction method onto Pd/TiO₂ catalysts for the selective hydrogenation of succinic acid in aqueous-phase. *Catal. Today* **2014**, *235*, 127–133. [[CrossRef](#)]
22. Kang, K.H.; Hong, U.G.; Bang, Y.; Choi, J.H.; Kim, J.K.; Lee, J.K.; Han, S.J.; Song, I.K. Hydrogenation of succinic acid to 1,4-butanediol over Re–Ru bimetallic catalysts supported on mesoporous carbon. *Appl. Catal. A Gen.* **2015**, *490*, 153–162. [[CrossRef](#)]
23. Kang, K.H.; Hong, U.G.; Jun, J.O.; Song, J.H.; Bang, Y.; Choi, J.H.; Han, S.J.; Song, I.K. Hydrogenation of succinic acid to γ -butyrolactone and 1,4-butanediol over mesoporous rhenium–copper–carbon composite catalyst. *J. Mol. Catal. A Chem.* **2014**, *395*, 234–242. [[CrossRef](#)]
24. Liu, X.; Wang, X.; Xu, G.; Liu, Q.; Mu, X.; Liu, H. Tuning the catalytic selectivity in biomass-derived succinic acid hydrogenation on FeOx-modified Pd catalysts. *J. Mater. Chem. A* **2015**, *3*, 23560–23569. [[CrossRef](#)]
25. Ly, B.K.; Tapin, B.; Aouine, M.; Delichere, P.; Epron, F.; Pinel, C.; Especel, C.; Besson, M. Insights into the Oxidation State and Location of Rhenium in Re–Pd/TiO₂ Catalysts for Aqueous-Phase Selective Hydrogenation of Succinic Acid to 1,4-Butanediol as a Function of Palladium and Rhenium Deposition Methods. *ChemCatChem* **2015**, *7*, 2161–2178. [[CrossRef](#)]
26. Pary, F.F.; Tirumala, R.T.A.; Andiappan, M.; Nelson, T.L. Copper (i) oxide nanoparticle-mediated C–C couplings for synthesis of polyphenylenediethynyls: Evidence for a homogeneous catalytic pathway. *Catal. Sci. Technol.* **2021**, *11*, 2414–2421. [[CrossRef](#)]
27. Chatterjee, R.; Lidin, S.; Bhattacharyya, S.; Kuila, S.K. Structure, microstructure and photocatalytic properties of embedded spherical Cu nanoparticles on Cu₂O–SiO₂. *Mater. Chem. Phys.* **2021**, *263*, 124360.
28. Tirumala, R.T.A.; Gyawali, S.; Wheeler, A.; Ramakrishnan, S.B.; Sooriyagoda, R.; Mohammadparast, F.; Khatri, N.; Tan, S.; Kalkan, A.K.; Bristow, A.D. Structure–Property–Performance Relationships of Cuprous Oxide Nanostructures for Dielectric Mie Resonance-Enhanced Photocatalysis. *ACS Catal.* **2022**, *12*, 7975–7985. [[CrossRef](#)]
29. Hsieh, M.-H.; Su, Z.-H.; Wu, E.-T.; Huang, M.H. Photocatalytic aryl sulfide oxidation using 4-nitrophenylacetylene-modified Cu₂O crystals. *ACS Appl. Mater. Interfaces* **2023**, *15*, 11662–11669. [[CrossRef](#)] [[PubMed](#)]
30. Li, H.; Wu, P.; Li, X.; Pang, J.; Zhai, S.; Zhang, T.; Zheng, M. Catalytic hydrogenation of maleic anhydride to γ -butyrolactone over a high-performance hierarchical Ni–Zr–MFI catalyst. *J. Catal.* **2022**, *410*, 69–83. [[CrossRef](#)]
31. Huang, Z.; Barnett, K.J.; Chada, J.P.; Brentzel, Z.J.; Xu, Z.; Dumesic, J.A.; Huber, G.W. Hydrogenation of γ -Butyrolactone to 1,4-Butanediol over CuCo/TiO₂ Bimetallic Catalysts. *ACS Catal.* **2017**, *7*, 8429–8440. [[CrossRef](#)]
32. Mutschler, R.; Moiola, E.; Luo, W.; Gallandat, N.; Züttel, A. CO₂ hydrogenation reaction over pristine Fe, Co, Ni, Cu and Al₂O₃ supported Ru: Comparison and determination of the activation energies. *J. Catal.* **2018**, *366*, 139–149. [[CrossRef](#)]
33. Kacem, S.; Qiao, Y.; Wirtz, C.; Theyssen, N.; Bordet, A.; Leitner, W. Supercritical carbon dioxide as reaction medium for selective hydrogenation of fluorinated arenes. *Green Chem.* **2022**, *24*, 8671–8676. [[CrossRef](#)]
34. Pang, J.; Zheng, M.; Wang, C.; Yang, X.; Liu, H.; Liu, X.; Sun, J.; Wang, Y.; Zhang, T. Hierarchical Echinus-like Cu–MFI Catalysts for Ethanol Dehydrogenation. *ACS Catal.* **2020**, *10*, 13624–13629. [[CrossRef](#)]
35. Liu, H.; Chang, Z.; Fu, J.; Hou, Z. A CuZn–BTC derived stable Cu/ZnO@SiO₂ catalyst for ethanol dehydrogenation. *Appl. Catal. B Environ.* **2023**, *324*, 122194. [[CrossRef](#)]
36. Zhao, H.; Yu, R.; Ma, S.; Xu, K.; Chen, Y.; Jiang, K.; Fang, Y.; Zhu, C.; Liu, X.; Tang, Y.; et al. The role of Cu^{1–3} species in single-atom Cu/ZrO₂ catalyst for CO₂ hydrogenation. *Nat. Catal.* **2022**, *5*, 818–831. [[CrossRef](#)]
37. Li, X.; Pang, J.; Zhao, Y.; Wu, P.; Yu, W.; Yan, P.; Su, Y.; Zheng, M. Ethanol dehydrogenation to acetaldehyde over a Cu^{δ+}-based Cu–MFI catalyst. *Chin. J. Catal.* **2023**, *49*, 91–101. [[CrossRef](#)]
38. Xu, C.; Chen, G.; Zhao, Y.; Liu, P.; Duan, X.; Gu, L.; Fu, G.; Yuan, Y.; Zheng, N. Interfacing with silica boosts the catalysis of copper. *Nat. Commun.* **2018**, *9*, 3367. [[CrossRef](#)] [[PubMed](#)]
39. Zhang, H.; Tan, H.-R.; Jaenicke, S.; Chuah, G.-K. Highly efficient and robust Cu catalyst for non-oxidative dehydrogenation of ethanol to acetaldehyde and hydrogen. *J. Catal.* **2020**, *389*, 19–28. [[CrossRef](#)]
40. Yuan, X.; Chen, S.; Cheng, D.; Li, L.; Zhu, W.; Zhong, D.; Zhao, Z.J.; Li, J.; Wang, T.; Gong, J. Controllable Cu⁰–Cu⁺ Sites for Electrocatalytic Reduction of Carbon Dioxide. *Angew. Chem. Int. Ed.* **2021**, *60*, 15344–15347. [[CrossRef](#)] [[PubMed](#)]
41. Wang, H.; Zhao, W.; Rehman, M.U.; Liu, W.; Xu, Y.; Huang, H.; Wang, S.; Zhao, Y.; Mei, D.; Ma, X. Copper Phyllosilicate Nanotube Catalysts for the Chemosynthesis of Cyclohexane via Hydrodeoxygenation of Phenol. *ACS Catal.* **2022**, *12*, 4724–4736. [[CrossRef](#)]

42. Lan, F.; Zhang, H.; Zhao, C.; Shu, Y.; Guan, Q.; Li, W. Copper Clusters Encapsulated in Carbonaceous Mesoporous Silica Nanospheres for the Valorization of Biomass-Derived Molecules. *ACS Catal.* **2022**, *12*, 5711–5725. [[CrossRef](#)]
43. Yu, D.N.; Dai, W.L.; Wu, G.J.; Guan, N.J.; Li, L.D. Stabilizing copper species using zeolite for ethanol catalytic dehydrogenation to acetaldehyde. *Chin. J. Catal.* **2019**, *40*, 1375–1384. [[CrossRef](#)]
44. He, X.; Wang, Y.; Zhang, X.; Dong, M.; Wang, G.; Zhang, B.; Niu, Y.; Yao, S.; He, X.; Liu, H. Controllable in Situ Surface Restructuring of Cu Catalysts and Remarkable Enhancement of Their Catalytic Activity. *ACS Catal.* **2019**, *9*, 2213–2221. [[CrossRef](#)]
45. Sun, L.; Wang, Y.; Wang, C.; Xie, Z.; Guan, N.; Li, L. Water-involved methane-selective catalytic oxidation by dioxygen over copper zeolites. *Chem* **2021**, *7*, 1557–1568. [[CrossRef](#)]
46. Luo, H.Y.; Consoli, D.F.; Gunther, W.R.; Román-Leshkov, Y. Investigation of the reaction kinetics of isolated Lewis acid sites in Beta zeolites for the Meerwein–Ponndorf–Verley reduction of methyl levulinate to γ -valerolactone. *J. Catal.* **2014**, *320*, 198–207. [[CrossRef](#)]
47. Van de Vyver, S.; Odermatt, C.; Romero, K.; Prasomsri, T.; Román-Leshkov, Y. Solid Lewis Acids Catalyze the Carbon–Carbon Coupling between Carbohydrates and Formaldehyde. *ACS Catal.* **2015**, *5*, 972–977. [[CrossRef](#)]
48. Hu, M.; Wang, C.; Chu, Y.; Wang, Q.; Li, S.; Xu, J.; Deng, F. Unravelling the Reactivity of Framework Lewis Acid Sites towards Methanol Activation on H-ZSM-5 Zeolite with Solid-State NMR Spectroscopy. *Angew. Chem. Int. Ed.* **2022**, *61*, e202207400. [[CrossRef](#)] [[PubMed](#)]
49. Zhou, B.-C.; Li, W.-C.; Wang, J.; Sun, D.-H.; Xiang, S.-Y.; Gao, X.-Q.; Lu, A.-H. PO_4^{3-} coordinated Co^{2+} species on yttrium phosphate boosting the valorization of ethanol to butadiene. *Chin. J. Catal.* **2024**, *56*, 166–175. [[CrossRef](#)]
50. Gao, M.X.; Jiang, H.X.; Zhang, M.H. The influence of calcination temperatures on the acid-based properties and catalytic activity for the 1,3-butadiene synthesis from ethanol/acetaldehyde mixture. *Appl. Surf. Sci.* **2018**, *439*, 1072–1078. [[CrossRef](#)]
51. Winoto, H.P.; Fikri, Z.A.; Ha, J.-M.; Park, Y.-K.; Lee, H.; Suh, D.J.; Jae, J. Heteropolyacid supported on Zr-Beta zeolite as an active catalyst for one-pot transformation of furfural to γ -valerolactone. *Appl. Catal. B Environ.* **2019**, *241*, 588–597. [[CrossRef](#)]
52. Pang, J.; Yin, M.; Wu, P.; Song, L.; Li, X.; Zhang, T.; Zheng, M. Redispersion and Stabilization of Cu/MFI Catalysts by the Encapsulation Method for Ethanol Dehydrogenation. *ACS Sustain. Chem. Eng.* **2023**, *11*, 3297–3305. [[CrossRef](#)]
53. Pampararo, G.; Garbarino, G.; Riani, P.; Vykoukal, V.; Busca, G.; Debecker, D.P. Ethanol dehydrogenation to acetaldehyde with mesoporous Cu-SiO₂ catalysts prepared by aerosol-assisted sol–gel. *Chem. Eng. J.* **2023**, *465*, 142715. [[CrossRef](#)]
54. Morales, M.V.; Asedegbega-Nieto, E.; Bachiller-Baeza, B.; Guerrero-Ruiz, A. Bioethanol dehydrogenation over copper supported on functionalized graphene materials and a high surface area graphite. *Carbon* **2016**, *102*, 426–436. [[CrossRef](#)]
55. Cui, G.; Zhang, X.; Wang, H.; Li, Z.; Wang, W.; Yu, Q.; Zheng, L.; Wang, Y.; Zhu, J.; Wei, M. ZrO_{2-x} modified Cu nanocatalysts with synergistic catalysis towards carbon-oxygen bond hydrogenation. *Appl. Catal. B Environ.* **2021**, *280*, 119406. [[CrossRef](#)]
56. Yan, W.-Q.; Zhang, J.-B.; Zhou, R.-J.; Cao, Y.-Q.; Zhu, Y.-A.; Zhou, J.-H.; Sui, Z.-J.; Li, W.; Chen, D.; Zhou, X.-G. Identification of synergistic actions between Cu⁰ and Cu⁺ sites in hydrogenation of dimethyl oxalate from microkinetic analysis. *Ind. Eng. Chem. Res.* **2020**, *59*, 22451–22459. [[CrossRef](#)]
57. Wang, C.; Zheng, M.Y.; Li, X.S.; Li, X.Q.; Zhang, T. Catalytic conversion of ethanol into butadiene over high performance LiZnHf-MFI zeolite nanosheets. *Green Chem.* **2019**, *21*, 1006–1010. [[CrossRef](#)]
58. Li, X.; Pang, J.; Wang, C.; Li, L.; Pan, X.; Zheng, M.; Zhang, T. Conversion of ethanol to 1,3-butadiene over high-performance Mg-ZrO_x/MFI nanosheet catalysts via the two-step method. *Green Chem.* **2020**, *22*, 2852–2861. [[CrossRef](#)]
59. Li, X.; Zhao, Y.; Pang, J.; Wu, P.; Yu, W.; Yan, P.; Su, Y.; Zhai, S.; Zheng, M. Cu-Zr/SiO₂ catalysts featured by different Cu-Zr-Si coordinations for ethanol conversion to 1,3-butadiene. *Resour. Chem. Mater.* **2024**, *3*, 27–37. [[CrossRef](#)]

Disclaimer/Publisher’s Note: The statements, opinions and data contained in all publications are solely those of the individual author(s) and contributor(s) and not of MDPI and/or the editor(s). MDPI and/or the editor(s) disclaim responsibility for any injury to people or property resulting from any ideas, methods, instructions or products referred to in the content.